ACS APPLIED ENERGY MATERIALS

www.acsaem.org
Article

Evolution of the Electrochemically Active Interface between a Li-Metal Anode and a Single-Crystal LLZO under Mechanical Loads

Diana Avadanii,* Steffen Ganschow, Stefan Mück, Markus Stypa, Dominik Kramer, Christoph Kirchlechner, and Reiner Mönig*

Cite This: https://doi.org/10.1021/acsaem.6c00908
Read Online

ABSTRACT: Batteries with solid electrolytes promise increased energy density and improved safety by pairing a high-capacity anode with a non-flammable, solid-state electrolyte ($Li_{6.5}La_3Zr_{1.5}Ta_{0.5}O_{12}$, LLZO). The bottleneck in the development of solid-state batteries remains the anode-electrolyte interface (Li|LLZO) interface, a dominant source of degradation and capacity loss due to the development of voids, and impurity segregation during discharge. This study presents direct, in situ, and quantitative observations of the electrochemically active area during anodic Li-metal stripping at initial current densities between 0.007 and 3.8 mA/cm^2 and loads up to ~7 MPa. The transparency of the single-crystal LLZO and the reflectivity of the Li-metal under visible-light microscopy enable these experiments. The void morphology and size vary with the initial current density: for the same charge, low rates lead to fewer, but larger voids compared to higher rates. Very slow stripping rates lead to angular and faceted voids. Stripping at high current densities generates a greater density of voids, and thus, an accelerated loss of the electrochemically active area. Applying a compressive load delays void growth, but can only mitigate loss of contact at the lowest rate. This study presents experimental evidence demonstrating the impact of current density and load on Li electrochemical stripping and provides information for interface engineering, numerical simulations, and charge-discharge protocols for solid-state batteries.

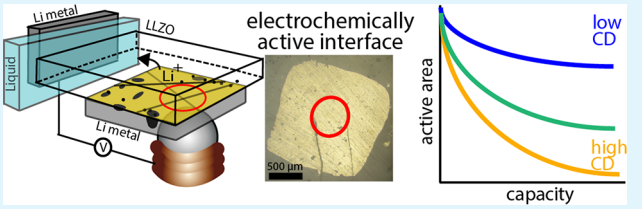

KEYWORDS: *electrochemically active interface, solid-state batteries, voids, interface degradation, Li-metal stripping*

INTRODUCTION

Solid-state batteries (SSBs) have been a focus for research and development in the past decades in both academia and industry due to their improved theoretical energy and power density, and safety compared to the widely used battery technologies with a liquid electrolyte.[1] Replacing the graphite anode with a pure lithium (Li) or a Li-rich alloy enables higher energy densities in SSBs compared to conventional lithium-ion batteries. For example, for the same cathode material, replacing the graphite anode and liquid electrolyte with a Li-metal anode and sulphide-based solid-state electrolyte (SE) increases the specific energy of a cell from 264 to 393 Wh/kg, and the volumetric energy density from 635 to 1143 Wh/L.[2] Research efforts to engineer solid-state batteries with a metal anode that are reliable over many charge-discharge cycles have focused on improving the ionic conductivity of the solid electrolyte,[3,4] the microstructure and diffusivity within the metal anode,[5−7] the adhesion between the metal and the solid-electrolyte,[6,8] and the battery architecture (e.g. interlayers,[8−11] 3D electrolyte framework[12−14]). These research efforts spanning Li-metal and Na-metal solid-state batteries, recently summarized in comprehensive reviews,[1,15] aim to provide an engineering solution to the key outstanding challenge for solid-state batteries with an alkali metal—loss of contact at the metal-electrolyte interface—leading to increased cell resistance, heterogenous current flux, and initiation of fracture in the solid electrolyte due to electrodeposition (i.e., "dendrites").[1]

In a solid-state battery with a metal electrode, interface processes underpin degradation at the anode. Ionic transport through the solid-state electrolyte requires electrochemical stripping (discharge) and deposition (charge) of Li (or sodium, Na).[2] During Li stripping, irreversible interface damage leads to increased cell impedance, followed by the propagation of Li-filled cracks in the solid-electrolyte ("dendrites") during deposition, and short circuit.[1] A wide array of studies attribute this interface damage to loss of contact resulting from void formation,[16,17] whereas a smaller subset propose the segregation of secondary phases.[18−20] Studies document an increase in cell voltage (nominally attributed to contact loss) even in cells cycled under stack pressures (≥5 MPa)[21−25] significantly higher

Received: March 21, 2026
Revised: June 13, 2026
Accepted: June 15, 2026

than the stress corresponding to the dominance of creep contributions to strain in bulk Li at room temperature (≈0.2–1.5 MPa).[26,27] At the electrochemically active interface (i.e., Li|SE), at the instant of stripping, practically every stripped metal atom generates a vacancy.[17,28] If the local current density inserts vacancies faster than they can annihilate or diffuse into the bulk anode, the accumulation of vacancies leads to void growth at the interface, and thus local dewetting.[17,29−31] Some theoretical models predict that nano-scale voids formed due to vacancy accumulation would shrink during ideal (or "layer-by-layer") Li stripping, and propose instead that micro-scale voids are a result of impurities at the interface.[19,32] The same authors propose a model for contact loss that relies on precipitation of solutes from the Li electrode.[18,20]

Loss of contact at interfaces within solid-state batteries is by default a challenging phenomenon to study using direct methods, or deconvolute from cell-level measurements.[15] Operando/in situ direct observations of interfaces within SSBs rely on cell reconstructions using X-ray techniques,[23,25,29] or observing interfaces in cross section using microscopy techniques (visible light,[24,33] scanning electron microscopy, SEM, and focused ion beam microscopy, FIB,[24] transmission electron microscopy, TEM,[30,34] atomic force microscopy, AFM[35]). Operando indirect assessment of interfaces in SBBs, such as electrochemical impedance spectroscopy (EIS), monitors changes in the voltage of a cell with an applied alternating current, and calculate the impedances of the cell at various frequencies.[15,36] These studies rely on complex models for data analysis and interpretation in order to deconvolute the contribution of different transport processes (bulk, grain boundary, interface) or the geometric asymmetries of electrodes, and have limited sensitivity to early stages of void nucleation when the changes in resistance can be under the detection threshold.[16,17,36] Recently, operando electrochemical dilatometry has been applied to measure changes in electrode height during anodic stripping and to approximate the corresponding void volume.[31]

In this study, we leverage an optically transparent Li-ion conductor (a single-crystal LLZO) to directly track the electrochemically active area during anodic stripping of Li metal. To achieve this, we assemble cells with optically accessible electrodes and a separator soaked with liquid electrolyte to mitigate dendrite propagation from the counter electrode, resulting in the obstruction of the field of view and solid electrolyte damage as previously documented in LLZO single crystals.[37−39] Our experimental design overcomes previous challenges arising from variations in assembly protocols[40] and optically inaccessible interfaces. We observe Li stripping on the same Li|LLZO interface across a current-jump test of two orders of magnitude, and interrogate the impact of an applied load by tracking the same interface with a varying load of 0 at the edges, and a maximum of ∼7 MPa towards the centre. We demonstrate that the initial current density has a significant impact on void morphology and density at the electrochemically active interface, and thus, on the rate of degradation with increasing charge. We further show that an applied compressive load only delays the loss of contact, but generally does not prevent it. Our direct observations of electrode interfaces spanning a few mm^2 bridge observations of void growth at nano- and microscales[30,34,41] to observations at the cell level[23,24] and inform numerical simulations of void growth and loss of the electrochemically active area under realistic battery operating conditions.

■ EXPERIMENTAL SECTION

Materials

In our experiments, we use a single-crystal $Li_{6.5}La_3Zr_{1.5}Ta_{0.5}O_{12}$ (LLZO) sample crystallized using the Czochralski technique. Similar samples have been used in previous studies.[37−39,42−46] We cut the crystal inside an Ar-filled glovebox (MBraun, <0.1 ppm O_2, <0.1 ppm H_2O) using a diamond saw, and further polish it on all sides using grinding paper with decreasing roughnesses (P320, P2500, and P7000). We reuse the electrolyte single crystal (samples A−D in Table 1) for multiple cells, and we re-polish (P7000), and clean the samples with cyclohexane, dimethyl carbonate, and an oxygen plasma device (Diener) over 30 minutes before each cell assembly. The oxygen plasma device is attached to the Ar-filled glovebox.

Cell Assembly and In Situ Electrochemical Measurements

We directly image the electrochemically active area through a sapphire cell window, and the transparent LLZO single-crystal electrolyte. We use the same cell setup in two different configurations: (a) without an applied load on the stripping anode, and (b) with an applied load,

Table 1. Details of Experiments and Corresponding Supplementary Videos and Figures

LLZO sample	LLZO size [mm]	cell	$A_{\perp 0}$ [mm^2]	I [μA]	j_0 [mA/cm^2]	P [MPa]	$P_{\perp max}$ [MPa]	video/figure
A 250702	2.8 × 3 × 1.1	2	2.65	−26.5	−1	2.2	0	SV1, S2
B 250703	3 × 2.3 × 0.9	2	2.6	−100	−3.84	3.4	0	SV2, S3
		3_I	1.7	− 0.3	−0.017	3.6	0	SV3, S4
		3_{II}	≈ 1.1	−30	≈ − 2.7	3.6	0	SV4, S5
		5	2.85	−2.85	−0.1	3.6	0	SV5, S6
C 250725	4.12 × 2.17 × 1.3	2_I	4.3	−0.3	−0.007	3	4.7	SV6, S9, S10
D 250807	4.4 × 4.1 × 1.6	2	3.7	−37	−1	2	6.5	SV7, S11, S12
		3	3.6	−3.6	−0.1	2	7.4	SV8, S13
		4	3.45	−17	−0.5	2	7.6	SV9, S14, S15
		5	5.7	−200	−3.5	2	5.7	SV10, S16

[a]We report the size of the solid electrolytes (labeled A, B, C, D), the cell number assembled with that specific LLZO crystal, the area of the electrode under observation, $A_{\perp 0}$, the applied galvanostatic current, I, the resulting current density according to the area measured in OCV after sample assembly, j_0, the load, P, on the cell, and the maximum perpendicular load, $P_{\perp max}$, on the electrode under direct observation (Figure 1). As detailed in the Experimental details section, the same LLZO sample has been used for multiple cells. In this Table, we report only experiments included in the data analysis. Some additional experiments are only reported in Supplementary Materials due to noise in the measurement and contamination during sample preparation.

https://doi.org/10.1021/acsaem.6c00908
ACS Appl. Energy Mater. XXXX, XXX, XXX−XXX

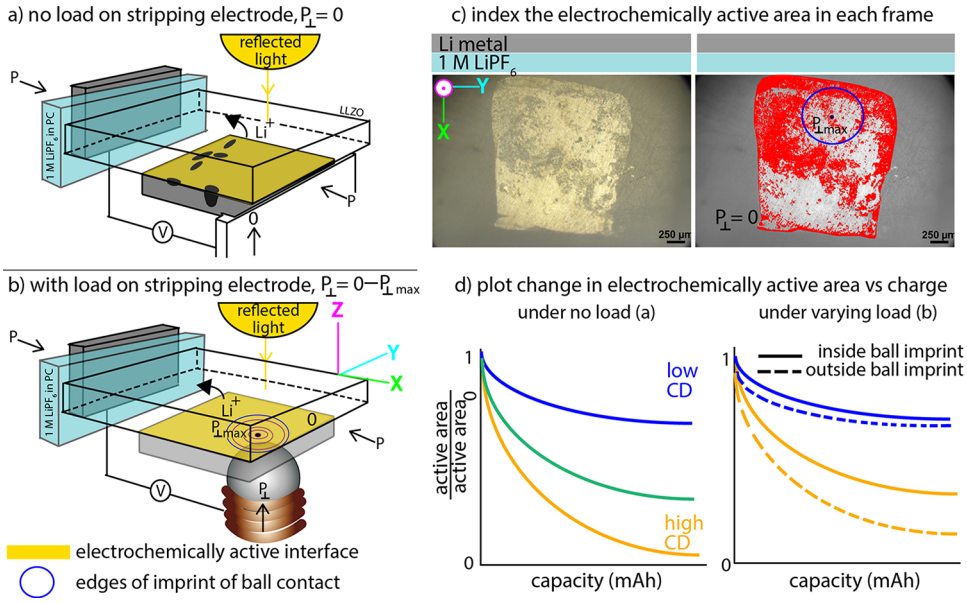

Figure 1. Schematic of the experimental setup in this study using a transparent single-crystal LLZO and perpendicular electrodes, resulting in a Li|Liquid|LLZO⊥Li cell. We track the electrochemically active area under (a) no load, including no cell-clamping load and (b) applied load, $P_{\perp}$, using a spring-loaded Ni ball. This experimental setup is also presented in Figure S8. (c) We use the pixel indexing workflow detailed in Figure S1 to index bright pixels, which we assign to the electrochemically active area. For samples under a point load, we find the area under the load by mirroring images after cell disassembly, as detailed in Supplementary Materials for each cell. (d) We track the evolution of the electrochemically active area with respect to the first frame under no load, as in diagram (a) and the evolution of the area inside and outside the point load in diagram (b) under a range of initial current densities (CD).

$P_{\perp}$, on the stripping anode (Figure 1). We make the Li⊥LLZO interface by melting Li metal (Alfa Aesar, 99.9%) on a hot plate and allowing it to cool to room temperature. We expect that this sample preparation routine results in a Li-metal electrode with relatively coarse grain sizes (100–200 µm).[41,47] For the counter electrode, we press freshly rolled Li metal on a Ni foil, and separate it from the SE by using a Whatman separator soaked with a liquid electrolyte (1 M $LiPF_6$ in PC). We place the cell in between two plates connected by screws with loaded springs (Gutekunst) of known elastic spring constant of 1.398 $\frac{N}{mm}$. We measure the spring length after cell assembly and approximate the applied load, P, reported in Table 1. For the configuration in Figure 1a, we connect the electrode we observe via a Ni plate. For the configuration in Figure 1b, we use a Ni ball (3 mm diameter, Goodfellow) on a loaded spring of know elastic constant (1.398 $\frac{N}{mm}$, Gutekunst). We measure the spring length after cell assembly, and the diameter of the imprint of the ball on the Li-metal electrode after disassembly in order to estimate the maximum applied load, $P_{\perp max}$, on the stripping anode (e.g. Figure S9). This maximum load is only present in the centre of the point contact, as depicted in Figure 1. Variations in electrolyte thickness and spring loading with each cell assembly result in a range of maximum applied loads of 4.7–7.6 MPa as reported in Table 1. Upon cell disassembly, we mirror the image of the electrode interface in contact with the Ni sphere and overlap it with the first frame collected during OCV, in order to approximate the outline of the area under the sphere contact (Figures S9, S11, S13, S14, S16). This setup results in an inhomogeneous pressure distribution on the stripping electrode, with a maximum applied load directly under the ball contact, and none at the edges (Figure S8).

We use a potentiostat (CompactStat.e, Ivium Technologies B.V.) connected to the cell assembly under the light microscope to collect measurements under galvanostatic conditions (Table 1) and use the extended voltage range of the potentiostat (−10 to 10 V). We use Matlab to plot our data and synchronize the light microscopy observations with the electrochemical measurements. We use the Ivium potentiostat to perform benchmark characterisations of our unique cell setup. We use potentiostatic electrochemical impedance spectroscopy (PEIS) and apply a 10 mV sinusoidal perturbation around the OCV potential of each cell, after 20 minutes of OCV recording after cell assembly. The frequency ranged from 1 MHz to 1 Hz, with a recording of 11 points per decade (Figure S18).

Image Analysis

In order to track the electrochemically active area, we use a microscope with a parallel-light beam (Nikon Eclipse LV-UDM) in the bright field setting, and an objective with a large field of view and working distance (Nikon, Plan Fluor, WD 17.2). The microscope is placed on a tabletop vibration isolation platform (Minus K Technology). For these measurements, we use a custom made electrochemical cell with a sapphire window. We collect images using the NIS-Elements AR software simultaneously with electrochemical measurements, and use the NIS-Elements AR software to construct in situ videos for each cell. We image the electrodes before and after each cell assembly in the glovebox using a USB-connected light camera with a ring LED light. We use this light camera within the glovebox to document and report cell assembly, disassembly, and track the same electrode area from in situ light microscopy to electron microscopy imaging.

We analyze images collected in reflected light using a Matlab script to track dark pixels in each frame. We present the schematic of our analysis in Supplementary Materials, Figure S1. Our analysis uses a dynamic threshold and an iterative process for finding the best indexing for each set of frames. We chose as a region of interest (ROI) the visible edges of the electrode. Within this ROI, we use the enhanced red channel for each frame to generate logical masks for pixels that are at the dark tail end of the intensity distribution, become darker from frame to frame, and are darker than the mean in their local neighborhood. For experiments under a load, some dark pixels become brighter from frame to frame. In the final count, we subtract these brightening pixels. These logical masks are combined using the boolean operator OR to generate the final binary mask for each frame. We present the histogram for the first and the last frame, and the indexing

https://doi.org/10.1021/acsaem.6c00908
ACS Appl. Energy Mater. XXXX, XXX, XXX–XXX

of dark pixels in key frames in each experiment in Supplementary Materials. We present synchronized optical and electrochemical measurements, as well as their corresponding dark pixel indexing for each frame, in the Supplementary Videos. Similar binarization approaches using the red channel of visible-light images have also been used by Kazyak et al.[48] and Zhang et al.[49] for Li electrodes during stripping in solid and liquid electrolytes, respectively.[48,49]

SEM Imaging

For a subset of our electrodes, we inspect the voids at the end of the measurement using a scanning electron microscope (SEM, Merlin, Carl Zeiss AG). These observations are possible only for electrodes that developed a high density of voids as these lift off easily from the LLZO upon cell disassembly, as previously noted in other studies.[17,31,50] We lift out these electrodes using a stainless steel needle in the electrode corner to minimize deformation, as displayed in Figure S4, place them on carbon pads, and transfer them into the SEM using an air-free transfer system (EM VCT 100, Leica). We orient and image the electrodes in the SEM chamber in a similar position to their orientation before cell disassembly and start imaging using a wide field of view, which matches the field of view in light microscopy. This imaging protocol is documented in Figures S4, S5, S10, S14, and S15. We use the wide field of view to determine the electrode areas with no or little deformation for closer inspection (Figures S2, S4, S5a, S10a,b, S11, S12a,b, S14, S15b). We image the Li-metal interface using a standard Everhart-Thornley detector, a working distance of 6 mm and 12 mm, and acceleration voltages of 3, 10, and 20 kV for the incoming beam. We also use an Energy-Dispersive X-ray Spectroscopy (EDS) detector to investigate the interface of the peeled off electrode.

HIM Imaging

Additionally, for some of our samples, we use a helium-ion microscope (Orion Nanofab, Carl Zeiss AG, Germany) to image the lifted electrode. This technique has high sensitivity to light elements and enables us to image very thin Li structures that are challenging to observe with commonly used techniques such as SEM. For imaging, we used a helium gas pressure of 2.6×10^{-6} mbar and an accelerating voltage of 25 kV. The samples were transferred between our glovebox and the helium-ion microscope under argon using an air-free transfer system (EM VCT 100, Leica).

RESULTS AND DISCUSSION

In this study, we introduce a novel setup for directly tracking the electrochemically active area during the stripping of a Li-metal electrode. Figure 1 depicts our method to leverage an optically transparent single-crystal LLZO electrolyte and directly observe Li stripping under reflected light. Using an LLZO Li-ion conductor ensures that no secondary interphase is present at the Li|SE interface, as pristine Li metal and LLZO do not react.[51−53] In this setup, the electrode under observation has by design a smaller surface area compared to the perpendicular counter electrode located behind the liquid electrolyte. Thus, the area of the observed electrode determines the current density at the interface under investigation. Furthermore, using a single-crystal SE increases the homogeneity of ionic transport due to the absence of grains and grain boundaries. Still, in our experiments, sources of Li|LLZO interface heterogeneity exist as a consequence of (1) impurities, (2) LLZO roughness, (3) Li-metal microstructure, (4) variations in adhesion (i.e., voids present after cell assembly). The surface of garnet solid electrolytes with various dopants has been successfully cleaned using chemical etching,[52] heating to 500 °C in an O_2 atmosphere,[54] or Ar atmosphere.[55] We use mechanical polishing and an oxygen plasma cleaner attached to the glovebox to remove surface contaminants that decrease wetting and hence, increase cell resistance (e.g. Li_2CO_3, LiOH[52,54,55]) from the LLZO surface (see Experimental Section). These steps are performed before each cell assembly. We use freshly rolled Li metal to fabricate electrodes with 70–150 μm thicknesses, which we press and melt onto LLZO single crystals. Consequently, all of the electrodes develop an oxide layer (passivation layer containing Li_2O,Li_2CO_3, LiOH, Li_3N),[34,49,53,56,57] which is ubiquitous for Li-metal, even under ultra-high vacuum conditions.

During stripping, dark patches appear on the observation plane—the interface between the Li metal and the LLZO (Figure 1a). In this study, our working interpretation is that these dark patches correspond to the loss of electrochemical contact and we use an image-analysis routine to index the dark pixels in each frame, thereby tracking the electrochemically active area (see Figures S1 and 1c). The first frame of each measurement corresponds to open-circuit voltage (OCV) conditions and in this frame, we interpret the contrasting dark areas as pre-existing imperfections of the interface, such as impurities, scratches, and pre-existing voids after interface formation. Therefore, the dark pixels indexed in the first frame correspond to the starting interface fraction that is electrochemically inactive in each experiment. As the effective applied current density increases during stripping, we use the electrode area measured in OCV, A_0, after cell assembly to calculate the initially applied current density, j_0 (Table 1). In subsequent frames, we directly track the electrochemically active area under galvanostatic conditions, and compare this area with the first frame. Therefore, our indexing of dark pixels serves as a proxy for the loss in the electrochemically active area, and is agnostic to the contribution of underpinning mechanisms (void formation or impurity segregation). This approach is consistent with previous numerical and experimental studies demonstrating that both impurities and voids can block the Li flux to the interface.[1,32,58] Note that this approach implies that the effective current density increases during Li stripping. Hence, we use j_0 to distinguish between cells. We aim to circumvent cell-to-cell variations in applied load by using a spherical contact, such that *for the same electrode* the load varies from 0 to $P_{\perp max}$ as drawn in Figure 1b. Similarly, we use a current-density jump test to appraise changes on the same electrode. Further details can be found in the Experimental Section and Supplementary Materials. In the following sections, we appraise the impact of the initially applied current density, j_0, and load, $P_\perp$, on the electrochemically active area during galvanostatic Li stripping.

Impact of Initial Current Density

We test the influence of the initially applied current density, j_0, on Li-ion stripping on the same interface. Figure 2 presents a current-density jump test from $j_0 = 0.017$ mA/cm^2 over ≈ 63 hours to $j_0 = 2.7$ mA/cm^2 over ≈ 10 minutes on the same electrode (Table 1). Figure 2a presents optical images of the electrochemically active interface after cell assembly in OCV (frame 1, stripping I) and at the end of Li stripping at $j_0 = 0.017$ mA/cm^2 (frame 1, stripping II) before changing the rate. During this stripping at relatively low current densities, the electrode develops overlapping dark circular patches around the edges, which reach diameters of 10–20 μm. The middle of the electrode contains fewer dark patches compared to the

https://doi.org/10.1021/acsaem.6c00908
ACS Appl. Energy Mater. XXXX, XXX, XXX−XXX

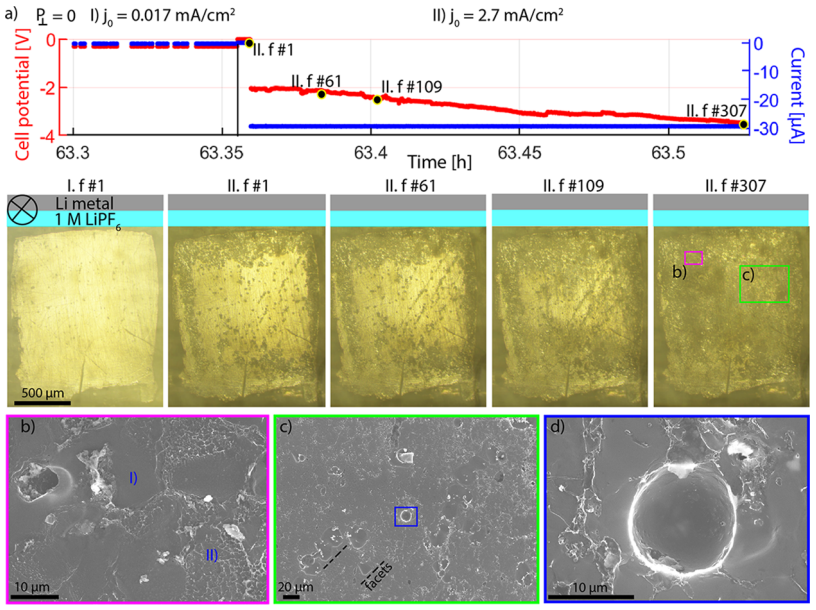

Figure 2. (a) In situ optical imaging of the same electrode undergoing Li-ion stripping at initial current densities of (I) $j_0 = 0.017$ mA/cm^2, and (II) $j_0 = 2.7$ mA/cm^2, respectively (Table 1). The optical imaging setup corresponds to the schematic in Figure 1a, and the perpendicular separator with liquid electrolyte and the Li-metal counter electrode are marked at the top of each frame. (b–d) Post-mortem SEM investigation after electrode peel off. Full imaging details are presented in Figures S4 and S5. (b) Voids formed during striping (I) have larger diameters > 10 μm and show coalescence. The second generation of voids corresponding to stripping (II) appears as regions with roughness with diameters <5 μm, between the larger voids developed during stripping (I). (c) Some large voids present facets, indicated by the black dashed lines. (d) Zoomed-in image of a larger void surrounded by smaller voids.

edges of the electrode. We interpret these dark patches as the imprint of voids, which develop during stripping at the Li|LLZO interface, and lead to the loss of contact at the interface and, thus, decrease light reflectivity in our light microscopy setup. We index the dark pixels appearing throughout the experiment and estimate the electrochemically active area in each frame, and thus calculate the current density corresponding to stripping II as $j_0 = 2.7$ mA/cm^2. At these significantly higher current densities, many more, much smaller patches appear simultaneously. Unlike the previously formed dark patches at the electrode margin, these new smaller patches seem more homogenously distributed on the interface (frames 61, 109, stripping II). We interpret these smaller dark patches as the imprint of much smaller voids generated across all of the remaining electrochemically active area, leading to loss of contact on the majority of the electrode interface (frame 307, stripping II). The high-degree of contact loss enables the post-mortem liftout of the electrode with minimal deformation, and subsequent inspection of the electrode side that was in direct contact with the LLZO. Figure 2b–d present SEM images of this Li electrode and demonstrate two distinct populations of voids: (i) with relatively smooth interior, with both circular and slightly faceted shapes, and diameters of 10–20 μm corresponding to the void population generated during stripping I ($j_0 = 0.017$ mA/cm^2, 0.018 mAh), and (ii) with rough edges, more angular morphology, and much smaller diameters <5 μm, generated during stripping II ($j_0 = 2.7$ mA/cm^2, 0.005 mAh).

The magnitude of the initial current density has a significant impact on interface degradation during Li-metal stripping under no applied load. Figure 3a displays the evolution of the electrochemically active area in electrodes stripped at varying initial current densities ($j_0 = 0.017$–3.8 mA/cm^2, Table 1, Figure S7). For the same amount of stripped charge, electrodes undergoing stripping under lower initial current densities lose less of their contact area (i.e., electrochemically active interface), compared to electrodes undergoing stripping at higher initial current densities. In Figure 3b, higher current densities lead to an increased voltage, in line with increasing ohmic resistance. In our setup, the cell voltage is impacted by (1) fresh Li deposition on the counter electrode, (2) loss of the electrochemically active area on the observed electrode, (3) solid-electrolyte interphase (SEI) formation on the electrode in contact with liquid electrolyte, (4) overall ohmic cell resistance. While we can not deconvolute the impact of these factors on the voltage, the synchronized electrochemical and optical measurements reveal that after an initial increase in voltage with decreasing electrochemically active area, the voltage becomes less dependent on the ongoing interface degradation (see Supplementary Videos). Note that the data presented in Figure 3b correspond to the cell setup depicted in Figure 1a, in which the electrode under reflected light is under no applied load, and the counter electrode is clamped behind the liquid electrolyte. In this cell configuration, there is none or little mechanical load on either electrode. Thus, the electrical contact between the Ni wiring and the Li metal is under none or little mechanical load, and could underpin some of the scatter in voltage curves in Figure 3b. However, the galvanostatic conditions ensure a constant current through the electrodes and electrolytes. Recent studies document a non-linear increase of cell resistance during Li-metal stripping, which they attribute to the interplay of bulk and surface diffusion of Li atoms.[31,59] Zaman et al.[59] use three electrode measurements in a symmetrical Li|LLZO|Li

https://doi.org/10.1021/acsaem.6c00908
ACS Appl. Energy Mater. XXXX, XXX, XXX–XXX

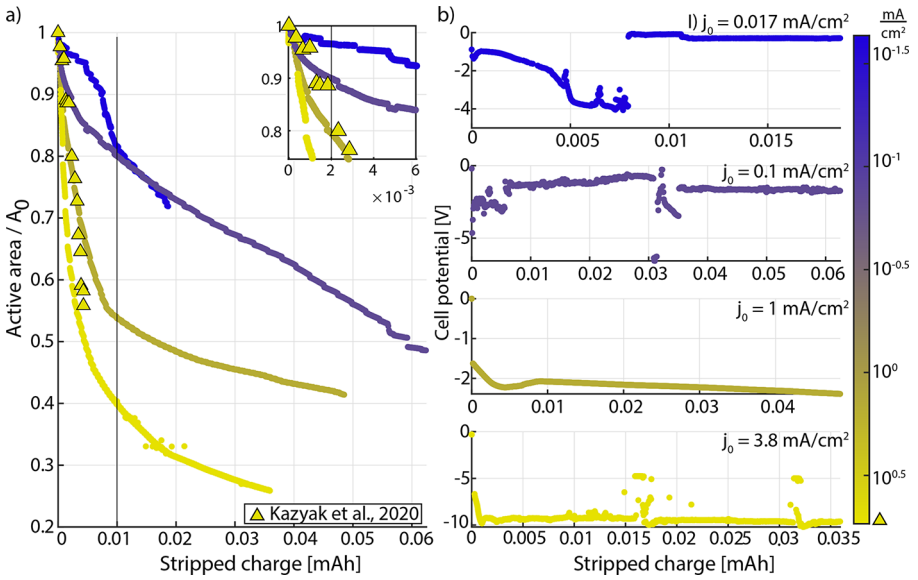

Figure 3. (a) Evolution of the electrochemically active area, A, normalized by the electrochemically active area in OCV, $A_{\perp 0}$, for Li-metal electrodes under galvanostatic stripping at different initial current densities, j_0, and no load on the observed interface (setup in Figure 1a). For comparison, we plot data reported by Kazyak et al. at 4 mA/cm^2 using triangle symbols.[48] We present frames corresponding to a stripped charge of 0.002 and 0.01 mAh in Figure 4. (b) Recorded cell voltage corresponding to each experiment in panel a. Note the different y-axis values, and the logarithmic color scale corresponding to j_0 for each experiment.

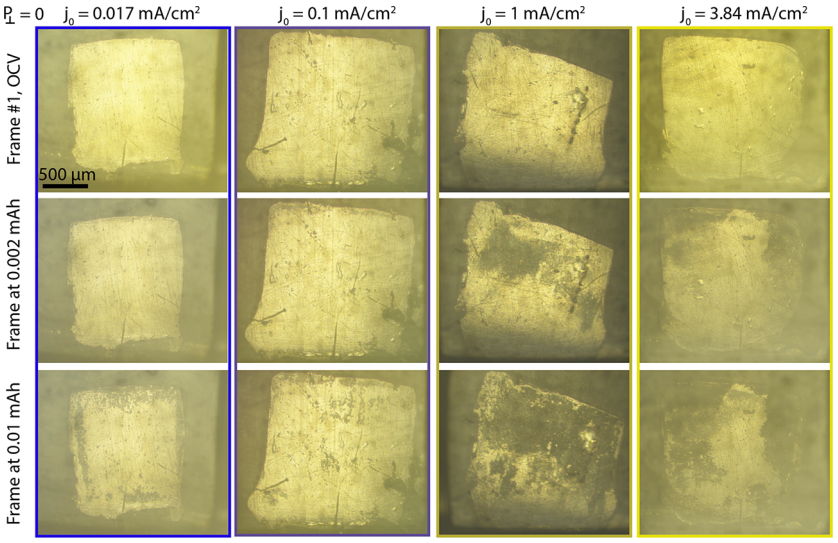

Figure 4. Selected frames corresponding to the first frame (OCV) in the first row and to a stripped charge of 0.002 and 0.01 mAh in Figure 3 for each experiment. The frames are unprocessed and reported on the same scale bar. The liquid electrolyte and the counter electrode are on the top of each frame, similar to the convention used in Figure 1c.

cell to deconvolute the different contributions to the flat voltage profile recorded for the overall cell. The authors demonstrate that the stripping voltage increases sharply with capacity until about 1.2 mAh/cm^2, after which there is a slowing down in the voltage increase with capacity.[59] Schall et al.[31] also use a symmetrical Li|LLZO|Li cell to demonstrate that the change of cell resistance with increasing void volume follows a function with a sharp inflection, almost similar to a step function, rather than a linear dependency (see their Figure 4).[31] In cells using a single-crystal LLZO and parallel electrodes, previous studies have also documented fluctuating voltage values up to 10 V,[38,42,44] which we attribute to the lower ionic conductivity of the single-crystal (0.25 mS/cm) compared to an LLZO pellet (0.63 mS/cm) and the higher sensitivity of the measurement to the surface finish and applied load, as measured by

https://doi.org/10.1021/acsaem.6c00908
ACS Appl. Energy Mater. XXXX, XXX, XXX−XXX

Reisecker et al. [38] We suggest that the large voltages at high current densities are a direct consequence of the large cell resistance and imposed galvanostatic conditions. Thus, the potential required for electrolyte decomposition (4 V against Li metal)[46,60] might not be available at the interface.

We present the electrochemically active area of electrodes having undergone the same amount of Li-ion stripping under different initial current densities in Figure 4. At a stripped charge of 0.002 mAh (insert in Figure 3a), electrodes stripped under low initial current densities (j_0 = 0.017 and 0.1 mA/cm^2) present a low density of voids at the edge closer to the counter electrode (see schematic and annotation in Figures 1 and 2). By contrast, electrodes stripped under high initial current densities (j_0 = 1 and 3.8 mA/cm^2) present smaller voids distributed over a much larger area of the electrode. With progressive stripping, at a charge of 0.01 mAh, the electrode stripped at the lowest initial current density (j_0 = 0.017 mA/cm^2) develops voids only close to electrode edges, with distinct radii of ≈ 10–20 μm. However, at this same charge, the electrode stripped at j_0 = 0.1 mA/cm^2 develops distinct voids in the center of the sample, along with voids on the edge of the sample closest to the counter electrode. The electrodes stripped at high initial current densities (j_0 = 1 and 3.8 mA/cm^2) keep developing small voids that agglomerate and form large areas of degradation of the electrode interface.

Void Development without External Load

Our observations highlight that void morphology and distribution depend on the initial current density for solid-state interfaces. During stripping at the ideal Li|LLZO interface, a vacancy and an electron are generated in the metal anode, while a Li ion moves into an available lattice site in the LLZO.[17,61] These vacancies rely on Li self diffusivity to either annihilate at grain boundaries, dislocations, or diffuse (creep) into the bulk metal. Void formation is underpinned by the coalescence of vacancies in supersaturated regions, and preferentially occurs around pre-existing defects such as dislocation structures, grain boundaries, or vacancy clusters (nanovoids). A larger driving force increases the vacancy concentration (for these experiments, j_0) and provides the required energy to overcome the penalty for heterogeneous nucleation around more defects, leading to a higher number of void nuclei within the volume. Conversely, a lower driving force enables heterogeneous nucleation with fewer nuclei, and favors significant growth as more vacancies are inserted. This balance between driving forces and void nucleation leads to the different void sizes with initial current density, as well as heterogeneous void distribution on the same electrode. We suggest that small current densities lead to void development at the electrode margins due to the lower energy penalty for delamination compared to the middle of the electrode-SE contact. Our experiments indicate that void nucleation and growth during stripping are compatible with frameworks for classical nucleation theory, as void radius decreases with increasing initial current density, similar to Lu et al.[24] and Zhang et al.[49]

In metals, the concentration of vacancies in thermal equilibrium, c_v, is directly related to temperature, T, and hydrostatic mechanical stresses, σ, via the relationship,

$$c_v \sim \exp\left(-\frac{E-\sigma\Omega}{RT}\right) \quad (1)$$

where E is the activation energy associated with vacancy formation, Ω is the atomic volume, and R is the gas constant.[62,63] In other words, for Li-metal under electrochemical stripping, higher current densities lead to elevated vacancy concentrations at the interface, and hence, greater tensile (positive) stresses. These increased stresses—the larger driving forces—enable void growth around pre-existing defects with high energy penalties. These tensile stresses provide the required stress for lateral void growth and dewetting of the LLZO. This leads to a void population distributed across the entire electrode interface for a large current density, including less favorable sites, such as the center of the interface. In our electrodes, the stress distribution at the interface is most likely non-uniform, hence the low currents (i.e., low stresses) enable void growth only at the most favorable sites, near the electrode perimeter.

Our results are compatible with similar observations in other solid-state systems and liquid electrolytes. Using cross-sectional observations of Li|argyrodite interfaces, Lu et al. also propose that void size is inversely proportional to the applied current density.[24] Additionally, observations of "pit formation" in Li-metal anodes paired with liquid electrolytes by Zhang et al. demonstrate that the radius of pits formed during stripping at a fixed capacity (0.2 mAh/cm^2) under a wide range of current densities (0.5–5 mA/cm^2) is inversely proportional to the overpotential and the applied current density.[49] However, unlike liquid systems in which the electrolyte fills the newly formed pits, void formation in solid systems directly leads to the decrease of the electrochemically active area.

Our in situ observations confirm that interface degradation at the early stages of stripping depends also on the initial current density, which can lead to discrepancies when using indirect techniques. Note that our experiments are galvanostatic and the effective current density increases proportionally with the decrease in the electrochemically active area. In our analysis, we refer only to the initial applied current density, j_0. For example, Kazyak et al.[48] use parallel electrodes that were aligned along the surface of LLZO to microscopically observe the stripping electrode away from the interface and estimate an apparent area, which we plot in our Figure 3a (see their Figure 10 in Kazyak et al.)[48] The authors use pulses of 4 mA/cm^2 and measure via EIS the capacitance in between each pulse, and remark that while the apparent electrode area decreases linearly with stripped charge, the capacitance decrease is non-linear.[48] The authors attributed this unexpected discrepancy to either inaccurate electrode area measurements, or chemical heterogeneities. In Figures 3 and S7 we confirm that for stripping under high current densities (>3 mA/cm^2) the electrochemically active area decreases non-linearly with stripped charge, similar to the capacitance decrease measured by Kazyak et al.,[48] and the decrease is closer to a hyperbola for high current densities. Schall et al.[31] coupled measurements of changes in anode height with cell resistance for experiments at low initial current densities (0.1 and 0.2 mA/cm^2). Similar to our direct observations, this approach revealed void growth in early stages of stripping, which were undetectable by EIS techniques.[17,31,36] The authors report voids with diameters > 10 μm, similar to our observations for Li-metal stripping under j_0 = 0.1 mA/cm^2.[31,50] These observations confirm that previous studies predicting void-free stripping for current densities up to 0.1 and 0.5 mA h/cm^2 (e.g., Krauskopf et al.)[17] have overestimated interface stability.

https://doi.org/10.1021/acsaem.6c00908
ACS Appl. Energy Mater. XXXX, XXX, XXX–XXX

Impact of an Applied Compressive Load

We use a Ni sphere loaded with a spring of known elastic constant to apply a load on the stripping electrode, as displayed in Figure 1b. In this setup, the load on the stripping electrode varies from 0 at the edges to $P_{\perp max}$ locally under the sphere as reported in Table 1 (Figure S8). We use mirrored images after cell disassembly to find the imprint of the Ni ball on the electrode and mark it with a circle on the in situ light microscope images (Figure 1c). We track the dark pixels corresponding to this area separately, and report the evolution of the electrochemically active area under a load varying from 0 up to $P_{\perp max}$ (Figure 1d). We chose a spatially varying load on purpose, in order to compare void morphology and evolution on the same stripping electrode, and minimize the impact of other variables such as differences in surface roughness (Figure S17) or preparation between cells. We also chose to align the spherical contact with electrode areas with elevated void density observed in the experiments without any load: the perimeter of the electrode for low current densities, and towards the middle of the electrode for high current densities. We track the electrochemically active area under and outside the Ni ball imprint on the electrode (see Supplementary Materials).

Voids developed under a local load are smaller compared to voids on a different area of the same electrode. Figure 5

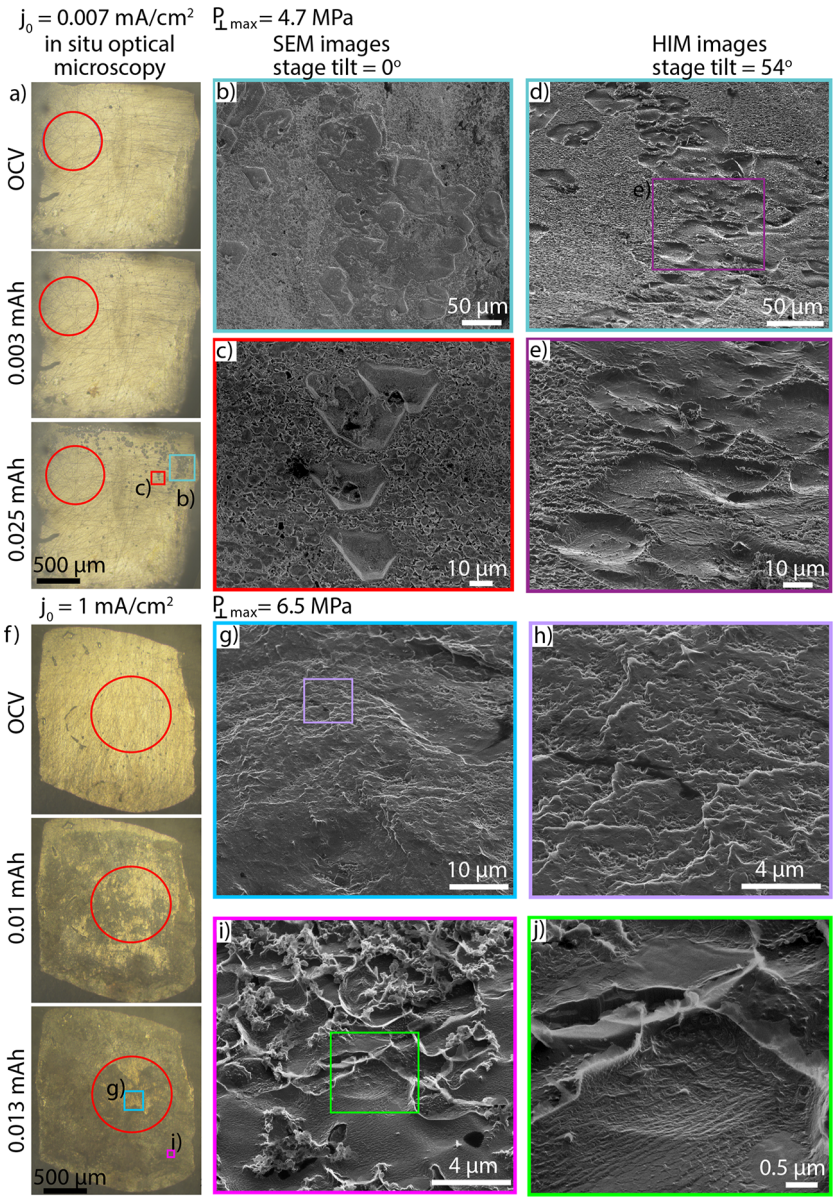

Figure 5. In situ imaging of electrodes stripped at low (panel a) and high (panel f) current densities, followed by electrode lift off and SEM (panels b, c) and HIM (panels d–j) imaging. Further details of cell disassembly and electrode imaging can be found in Figures S9–S12 and Table 1. The imaging setup corresponds to the schematic in Figure 1b and the area under the load is marked by the red circle. The liquid electrolyte and counter electrode are at the top of the frames, similar to the convention in Figure 1c. Note that the electrode in panels b–e is overprinted by oxide impurities as detailed in Figures S9 and S10. Images captured with a tilted stage emphasize the 3D roughness of voids in panels d–e, and g–j. Note that panels h and i are on the same length scale. The voltage curves corresponding to the charge annotated for each frame are presented in Figure 6c.

https://doi.org/10.1021/acsaem.6c00908
ACS Appl. Energy Mater. XXXX, XXX, XXX–XXX

presents experiments at low (0.007 mA/cm^2, 0.025 mAh) and high (1 mA/cm^2, 0.017 mAh) current densities, with maximum loads of 4.7 and 6.5 MPa on the electrodes. In Figure 5a, the electrode stripped under low current densities develops angular, faceted voids. While some facets can also be observed in voids presented in Figure 2c (j_0 = 0.017 mA/cm^2, 0.018 mAh), the voids in Figures 5b–e consistently present facets and a 3D development of voids with diameters of approximately 15–20 μm and an apparently flat aspect ratio. This faceting indicates that these voids developed within the Li grain interior, similar to voids with facets observed by Lang et al.[41] and Gao et al.[30] The development of facets is underpinned by energy minimization during the inhomogeneous and anisotropic Li adatom diffusion on different crystallographic planes of the elastically anisotropic bcc Li metal.[63,64] Note that for this electrode, lift off and SEM and HIM imaging was enabled by a second stripping at high current densities, resulting in impurity accumulation at the interface (Figures S9, S10). Figure 5f–j present images of the interface degradation during stripping at high current densities (1 mA/cm^2, 0.017 mAh), and postmortem investigations of the area under a local load ($P_{\perp max}$ = 6.5 MPa) and at the electrode edges ($P_\perp$ = 0). The area directly under the load presents roughness at much smaller length scales, and the imprint of the LLZO scratches are still observable on the metal electrode in Figure 5g (Figure S17). We present similar SEM images with marks on the Li electrode from the LLZO roughness for the area under a load for an electrode with j_0 = 0.5 mA/cm^2 (0.023 mAh) in Figure S15. The roughness in Figure 5h indicates void development on length scales <4 μm for the area under a load. By contrast, Figure 5i displays the area at the edge of the electrode with roughness on length scales >4 μm. As voids have expanded laterally, very thin (almost electron transparent) Li develops as void walls, and a second order roughness is imaged on the interior of the voids (Figure 5j). The very thin bright Li between voids in Figure 5j would be difficult to image with SEM because Li is almost transparent for electrons. The He ions used in HIM yield low energy electrons even on light elements such as Li and allow for the observation of very thin layers.

Loads up to 7.6 MPa on the stripping electrode mitigate interface damage with increasing charge, and do not completely suppress void formation. Figure 6 displays the evolution of the electrochemically active area in electrodes stripped at various initial current densities under a varying load across the same interface (Table 1). Similar to results under no load in Figure 3, for the same amount of stripped charge, electrodes undergoing stripping under lower initial current densities lose less contact with the LLZO compared to electrodes stripped at higher current densities. Using a load on the stripping electrode impacts the evolution of the electrochemically active interface (Figure 1b). Comparing Figure 6a,b we note that overall, for the same amount of charge, the areas under a varying load (i.e., within the red circle in Figure 7) preserve more contact compared to areas under no or very little load outside the edges of spherical contact. In other words, with increasing stripped charge, more dark pixels are added to the area outside the spherical load, compared to the dark pixel counts in the area directly under the load (marked with red circles in Figures 5, 7, 8). Furthermore, we observe that during these experiments, certain dark pixels brighten with increasing charge (see Supplementary Videos), leading to a decrease in the dark pixel count compared to the previous frame

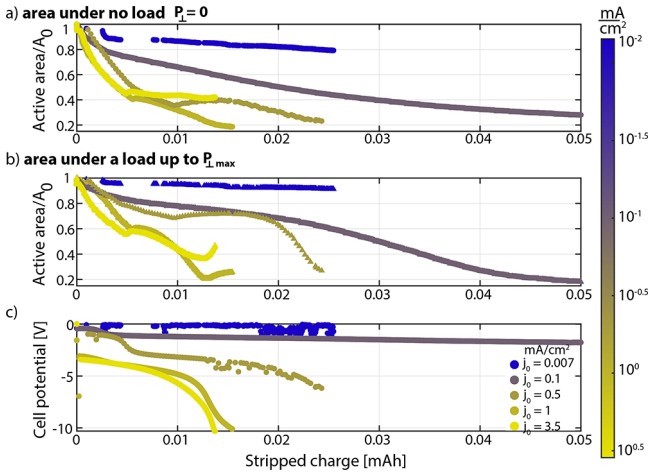

Figure 6. Evolution of the electrochemically active area, A, normalized by the electrochemically active area in OCV for Li-metal electrodes under galvanostatic stripping at different current densities and an applied load up to $P_{\perp max}$ = 4.7–7.6 MPa on the observed interface (Figure 1b). (a) Decrease in A compared to the first frame in OCV for the area of the electrode outside direct contact with the Ni sphere (Figure 1c, area outside the blue circle). (b) Decrease in A compared to the first frame in OCV for the area of the electrode directly under the Ni sphere (Figure 1c, area inside the blue circle). Note that panels a and b are on the same scales. (c) Recorded cell voltage for each experiment in panels a and b. Note the logarithmic color scale corresponding to j_0 for each experiment.

(Figure S1). This change of previously dark pixels into brighter ones results in an inflection in tracking the electrochemically active area with charge. We interpret the brightening of previously dark pixels as recovery of the interface contact beneath and around the area under a compressive load. In Figure 6c, higher current densities lead to an increased voltage, in line with increasing ohmic resistance and decrease of the area of the electrochemically active interface. Similar voltage curves increasing more abruptly for cells stripped under higher current densities have also been reported in previous studies.[21,25,38,50,59,65] Note that the voltage curves in Figure 6c corresponding to electrodes under a point load present less scatter compared to the ones in Figure 3b, due to the mechanical force between the Ni wiring and the Li electrode. Thus, we attribute the scatter in voltage curves in Figure 3b to the lack of a compressive force on the stripping electrode.

Under an applied load (<7.6 MPa), the magnitude of the initial current density dominates interface degradation at charges up to 0.005 mAh, after which the applied load has a significant impact on interface recovery. Similar to Figure 4, we present in Figure 7 the electrochemically active area of electrodes having undergone the same amount of Li-ion stripping under different initial current densities and an applied load. At a charge of 0.005 mAh (first row, Figure 7) electrodes stripped under low initial current densities (j_0 = 0.007–0.1 mA/cm^2) present a lower density of larger voids, mainly around the electrode edges, whereas electrodes stripped under high initial current densities (j_0 = 0.5–1 mA/cm^2), present an increased density of smaller voids at the electrode edges and middle. At a stripped charge of 0.01 mAh, the applied load enables distinguishable interface recovery during in situ monitoring (i.e., pixels that were dark in earlier frames become brighter) only in the cell with the

https://doi.org/10.1021/acsaem.6c00908
ACS Appl. Energy Mater. XXXX, XXX, XXX–XXX

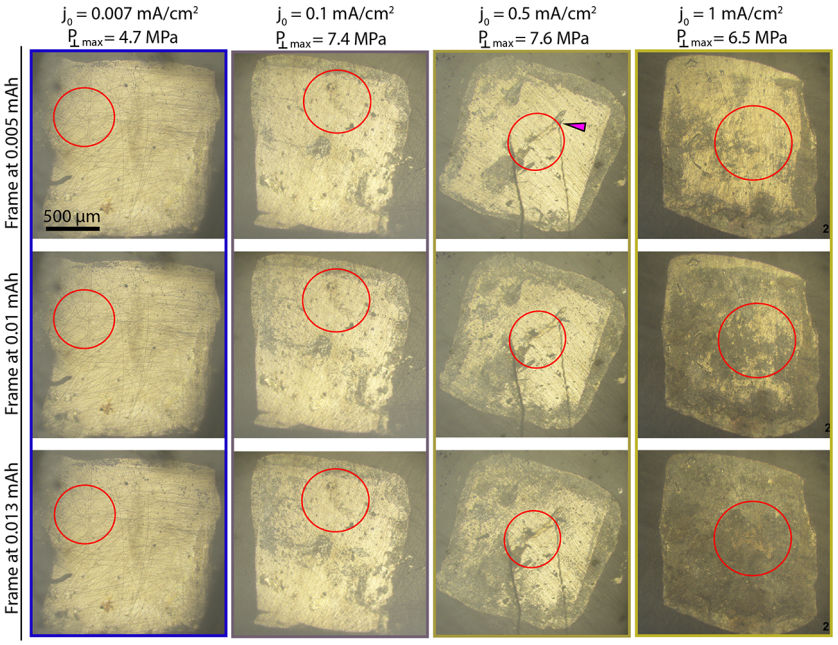

Figure 7. Selected frames corresponding to 0.005, 0.01, and 0.013 mAh of stripped charge in the first, second, and third row, respectively. The frames are unprocessed and reported on the same scale bar. The frames captured during in OCV can be found in Figure 5a for the electrode in the first column, and in Figures S13, S14, and S11 for the electrodes in the second, third, and fourth column, respectively. The magenta arrow points toward pixels that become brighter in subsequent frames. The area under the a point load up to $P_{\perp max}$ (Figure 2b) is marked by a red circle. The electrode area outside the red circle is under no load. The counter electrode and the liquid electrolyte are at the top of each frame, similar to the convention presented in Figure 1c.

highest $P_{\perp max}$ of 7.6 MPa. In Figure 7 the magenta arrow marks the dark pixels that brighten with increasing charge from 0.005 to 0.01 mAh. Additionally, Figure 8 demonstrates that the inflections observed in Figure 6a,b correspond to brightening pixels with increasing charge, which we interpret as interface recovery due to the applied load. Figure 8a presents an example of interface recovery after a rest period of 12 hrs of OCV, in which we observe brightening of pixels corresponding to the Li directly under load (Figure S14). Figure 8b,c present pixel brightening with increasing charge for electrodes stripped at high current densities (j_0 =1–3.5 mA/cm^2) under loads of up to 6.5 MPa.

Interface Evolution under a Load

We demonstrate that loads up to 7.6 MPa delay the onset of voids during electrochemical stripping in Li-metal on LLZO, but do not entirely mitigate void formation. The vacancy injection rate due to stripping at the interface is independent of the applied load. However, the vacancy concentration is lower in areas under compression (eq 1, Figure S8). Despite the compressive loads up to 7.6 MPa, we observe voids for all experiments, except the slowest rate (0.007 mA/cm^2, 0.025 mAh, Figures 5, 7, S9), where voids are not present in the region of maximum compressive load, $P_{\perp max}$. Note that voids do appear in areas equidistant from the counter electrode in Figure 5b,c. Voids require the presence of tensile stresses. Our observation of voids indicates that the number of vacancies injected into the interface at rates higher than 0.007 mA/cm^2 cannot be compensated by Li atoms during creep, i.e., metal diffusion driven by a stress gradient. This gradient relates to the difference in mechanical stresses between the outer lithium surface (compressive) and the electrochemical interface (tensile).

Even under a load up to 7.6 MPa, high initial current densities lead to a faster loss of the electrochemically active area. For a simple approximation, the ratio between the area of a circle and the volume of a hemisphere with the same radius, r, is inversely proportional to the radius ($\frac{\text{area}}{\text{volume}} \sim \frac{1}{r}$). Therefore, for the same total volume, smaller radii result in a greater surface area. Our observations demonstrate that for the same charge, high current densities enable the generation of more Li surface with much higher diffusivities, and thus the dominance of adatom diffusion on the void surface, compared to lower current densities in which bulk and grain boundary diffusion still play a significant role.[41] In other words, for the same amount of stripped charge, the higher surface-to-volume ratio generated at high current densities increases the contribution of adatom diffusion, which is much faster compared to bulk and grain boundary diffusion (surface > grain boundary > bulk diffusion).[17,66,67] These observations, provide direct evidence for previously suggested models emphasizing the role of surface adatom diffusion in Li|SE interface degradation.[17,24] With increasing charge, the significant interface degradation presented in Figures 4 and 6 leads to current constriction effects in cells, and locally elevated current densities.[17,36]

We attribute the observable interface recovery to Li-metal creep during both OCV (Figure 8a) and ongoing stripping (Figures 7, 8b,c). We observe significant recovery towards the end of stripping at high current densities (Figure 8b,c). At these high current densities, the electrochemically active interface does not decrease as fast towards the end of the stripping, and for the areas under a load the interface recovers during

https://doi.org/10.1021/acsaem.6c00908
ACS Appl. Energy Mater. XXXX, XXX, XXX–XXX

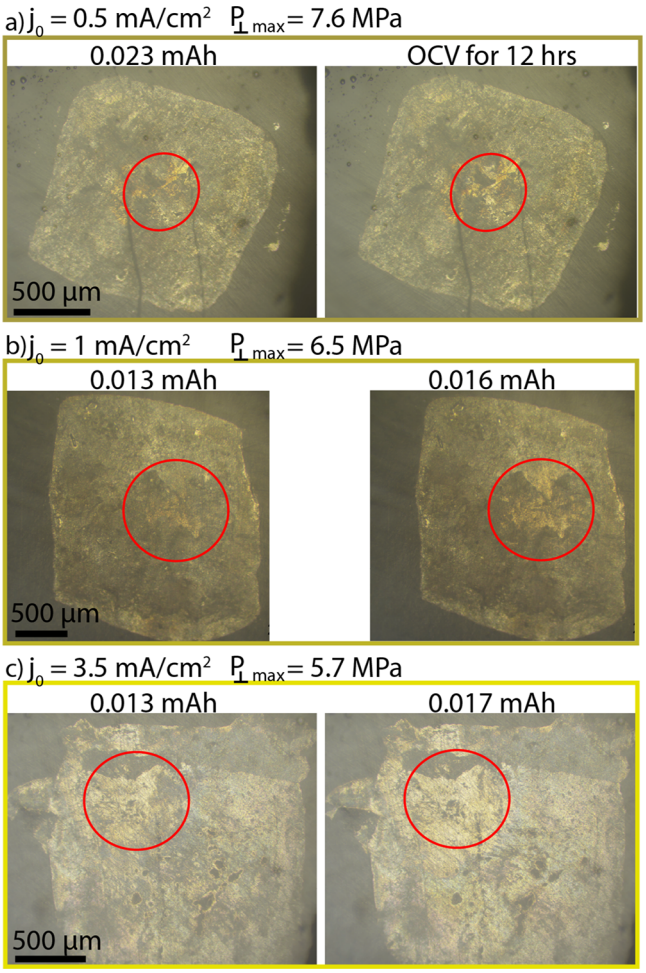

Figure 8. Selected frames displaying the impact of a load on the electrochemically active area. (a) Pixels become brighter (i.e., interface recovery) after a period of OCV. (b, c) Pixels become brighter with progressive stripping under high current densities. The area under load is marked by a red circle. The SEM investigation of the sample with j_0 = 0.5 mA/cm² after electrode lift off can be found in Figure S15. All images are reported on the same scale bar. The counter electrode and the liquid electrolyte are at the top of each frame, similar to the convention presented in Figure 1c.

stripping (Figure 6b). This recovery suggests that a more spatially homogenous insertion of vacancies (and generation of tensile stresses) over the electrode interface under high current densities is at least partially compensated by the yield and transient creep of the Li under the load. The limited interface recovery and void growth hint towards the impact of the small-scale mechanics and possible size effects in the mechanical strengthening of Li counteracting yield and creep at the interface.[27,64,68,69] While strain can easily be accommodated on the macroscale length of our electrodes, size-effects will play an increasingly greater role due the thinning of Li between growing voids. At room temperature, Li metal has a homologous temperature of 0.65, and displays mechanical behavior consistent with power-law creep with an exponent of approximately 6.5 and a rate-limiting mechanism controlled by lattice diffusion (dislocation climb), as well as a size effect in strain accommodation controlled by the aspect ratio of the deforming area.[27,68,69] According to compression creep experiments performed by Haslam et al., a Li-metal foils with aspect ratios greater or equal to 0.07 would reach steady-state deformation after approximately 30 minutes of loading at 5 MPa, and that samples with these aspect ratios easily accommodate large creep rates (Figure S8).[68] In our cells, the Li-metal undergoing deformation under the Ni ball has aspect ratios between 0.1 and 0.2. These aspect ratios imply that for the electrodes in our study, only the areas under the load for the electrodes with j_0 = 0.007–0.5 mA/cm² (Table 1) reached steady-state Li deformation prior to void formation, and during 12 hours OCV (Figure 8a). Our direct observations confirm that an applied load alone does not entirely mitigate voids at the interface, as previously discussed by Zaman et al.[59]

Our results directly inform numerical studies calculating the boundaries of regimes of stripping without void formation. Models of Li self-diffusion indicate that under an equilibrium current density, the vacancy insertion balances vacancy diffusion and annihilation and thus, no voids (i.e., new surfaces) form.[17] Using this vacancy concentration balance, Krauskopf et al.[17] estimate this equilibrium current density in the range of 0.05–0.2 mA h/cm² at room temperature, under no stack load.[17] Lu et al.[24] use DFT to predict stable stripping at current densities up to 6 mA/cm² for 1 mA h/cm² and no stack pressure (see their Figure 2[24]), which we do not observe, suggesting that experimental inhomogeneities (e.g. interface impurities, Li metal microstructure) are not captured by the aforementioned studies. Agier et al.[32] couple power-law creep of Li metal with electrochemical stripping and predict that no void would develop diameters exceeding 10 µm and that loads up to 1.5 MPa would stabilise void growth, which we do not observe (Figures 5). Recent phase-field based predictions by Barai et al.[50] of void formation at 0.1 mA h/cm² and no stack load indicates void growth with diameters greater than 8 µm after ≈ 5 hours. Their predictions, including those of void formation during stripping under a stack load up to 8 MPa, match well with our experimental observations (Figures 4, 7, 8). For this simulation, the authors assumed pristine Li surfaces with a diffusivity 2000 times greater than bulk diffusivity.[50] The agreement between our experiments and their simulations suggests that the large discrepancies between surface and bulk diffusivity in Li contribute to void growth even under a load. Recent numerical simulations exploring the interplay between different types of surface Li diffusion and overpotential in the loss of the electrochemically active area match qualitatively with our observations in Figures 3 and 6.[70] Furthermore, our observation of void facets for current densities <0.02 mA h/cm² have not been predicted by numerical studies and further emphasize the role of heterogeneities in surface energy and diffusivity in void growth.

Microstructural and Chemical Factors Impacting the Interface

Our experimental design minimizes the impact of microstructural and chemical factors impacting the evolution of the electrochemically active area. We assume that the LLZO remains a constant in our experiments, despite small differences in surface roughness or residual contaminants after sample preparation. Similarly, our Li-metal electrodes are prepared using the same rolling and cooling routine, and we expect consistent microstructures amongst the observed electrodes (large grain sizes in the 100–200 µm range).[41,47] Thus, our observations

https://doi.org/10.1021/acsaem.6c00908
ACS Appl. Energy Mater. XXXX, XXX, XXX–XXX

are only sensitive to the applied current density, load, and variations in the passivation layer or contaminants in the Li electrodes. Operando direct imaging using X-rays in Li|LLZO|Li reveals void formation at small current densities (<0.02 mA h/cm^2) in hot spots correlated with microstructure of the LLZO pellet.[29] While electrolyte porosity, and presence of grain boundaries might influence void formation, we demonstrate that the initially applied current density has a significant impact on interface degradation and generation of hot spots for interface detachment. Note that very few of the voids we present follow the roughness on the surface of the electrolyte. For example, while some of the voids in the panels in Figure 2a and c follow residual scratches on the LLZO, the voids developing in Figure 7 (third column) do not follow the deeper scratches introduced with a diamond pen on the LLZO (Figure S15). Lewis et al.[23] also present heterogeneous decrease in the electrochemically active area using X-ray techniques on Li|LSPS|Li cells, and note that void formation is independent of surface roughness, similar to our observations in LLZO.[23] However, Lee and Sakamoto[65] use LLZO pellets with different surface roughnesses to demonstrate that a flatter SE enhances the stripping capacity of the Li metal anode.[65] We demonstrate that variations in surface roughness of the LLZO have a minor impact on void development. We suggest that for Li metal against LLZO, inhomogeneities in electrode application and in interface formation (different loads and temperatures), which influence Li metal wetting, as well as variations in electrode thickness, chemical purity, and the passivation layer play a significant role in generating hot spots for interface degradation. For example, in our experiments at slow rates, the edges of the electrodes (locally thinner) represent hotpots for contact loss.

Both impurity segregation and void growth are simultaneously occurring and lead to loss of contact and increased cell voltage. In our experiments, these impurities appear brown and black under light microscopy upon cell disassembly and also leave residue on the LLZO after electrode lift off (Figures S9–S14). Note that not all cells present detectable residual impurities upon cell disassembly as documented via light microscopy in Supplementary Materials. EDS measurements (Figures S10, S12, S15) on peeled off electrodes indicate an O, C, and N enrichment correlated with these impurities on some of the electrodes. Noteworthy, in one experiment, the impurity segregation at the interface was detected only after a current-jump test (Figure S9). We suggest that our Li-metal electrodes become enriched in C- and N-based impurities during melting of the electrode on the LLZO due to the trace amounts present in the glovebox. We mitigate against this contamination by running frequent glovebox regeneration protocols, as well as melting larger amounts of Li in the glovebox with the aim to trap residual N and C products. Becker et al.[58] also report a dark film left on the solid-electrolyte after cell disassembly, which they attribute to Na-rich impurities.[58] Vema et al.[20] document oxide-rich impurities depositing during stripping of at Li|LLZO and propose a model for contact loss solely due to impurity segregation.[18,20,32]

■ CONCLUSIONS

Our experimental strategy focuses on minimizing variability (e.g., electrolyte microstructure, interface formation, anode composition) and observing electrochemical stripping on a simplified system relevant for SSBs with oxide electrolytes. We document the development of high degrees of inhomogeneity on the same interface, which we expect to be enhanced within cells with high technology-readiness level. The initial current density impacts both void morphology and void density at the electrochemically active interface. Very small current densities (<0.02 mA h/cm^2) lead to fewer, but larger voids, often with facets corresponding to crystallographic planes within the Li grains. Large current densities (>0.5 mA h/cm^2) lead to a greater number of voids of smaller sizes. Thus, for the same volume of removed Li, faster rates lead to a disproportionally faster loss in the electrochemically active area. These dynamics are still present when a load up to 7.6 MPa is applied on the stripping electrode. Applying a load mitigates and delays interface decoupling due to void formation. The external load generates a flux of lithium metal atoms to the interface, which is strained under tension due to vacancy injection. The resulting balance determines whether an external stack pressure can prevent void formation. Our observations further indicate that macroscale compressive loads cannot counteract the nanoscale stress fields that form during electrochemical stripping. Segregation of impurities at the interface also leads to further unrecoverable loss of the electrochemically active interface. We present a simplified system for investigating electrochemical stripping, which could be used as a benchmark in future numerical studies investigating interface degradation across a wide range of current densities, low stack pressures, and impacted by current constriction. Future improvements on our system include additional developments to apply a fixed or an oscillating load, as well as cells assembled with alloy anodes (e.g., Mg-Li alloys), interface coatings, and thinned and light-transparent LLZO pellets. Our results imply that future interface optimization of SSBs should be directed toward balancing surface (inside voids) and bulk diffusivities in the metal anode, as well as accommodating the local strains caused by vacancy injection at the interface.

■ ASSOCIATED CONTENT

Data Availability Statement

All data (in situ frames, electrochemistry) and code associated with image processing are available via KIT Open at the DOI 10.35097/rw9xx484k78jmm90.

Supporting Information

The Supporting Information is available free of charge at https://pubs.acs.org/doi/10.1021/acsaem.6c00908.

Diagrams depicting the methodology used in this study, and images of each cell assembly and disassembly (PDF)

Videos display the image analysis of the in situ frames (ZIP)

■ AUTHOR INFORMATION

Corresponding Authors

Diana Avadanii – *Institute for Applied Materials IAM, Karlsruhe Institute of Technology KIT, Karlsruhe 76344, Germany;* orcid.org/0000-0003-4534-1485; Email: diana.avadanii@kit.edu

Reiner Mönig – *Institute for Applied Materials IAM, Karlsruhe Institute of Technology KIT, Karlsruhe 76344, Germany;* orcid.org/0000-0003-1048-9973; Email: reiner.moenig@kit.edu

Authors

Steffen Ganschow – *Leibniz-Institut für Kristallzüchtung IKZ, Berlin 12489, Germany*; orcid.org/0000-0003-1328-1617

Stefan Mück – *Institute for Applied Materials IAM, Karlsruhe Institute of Technology KIT, Karlsruhe 76344, Germany; Karlsruhe Nano Micro Facility (KNMFi), Eggenstein-Leopoldshafen 76344, Germany*

Markus Stypa – *Leibniz-Institut für Kristallzüchtung IKZ, Berlin 12489, Germany*

Dominik Kramer – *Institute for Applied Materials IAM, Karlsruhe Institute of Technology KIT, Karlsruhe 76344, Germany*

Christoph Kirchlechner – *Institute for Applied Materials IAM, Karlsruhe Institute of Technology KIT, Karlsruhe 76344, Germany*

Complete contact information is available at: https://pubs.acs.org/doi/10.1021/acsaem.6c00908

Notes

The authors declare no competing financial interest.

■ ACKNOWLEDGMENTS

The authors thank Mr Edmund Böck for technical support in manufacturing the optical cell setup. We acknowledge the support of the Karlsruhe Nano Micro Facility (KNMFi, www.knmf.kit.edu), a Helmholtz Research Infrastructure at the Karlsruhe Institute of Technology, for facilitating using the He-ion microscope.

■ REFERENCES

(1) Janek, J.; Zeier, W. G. Challenges in speeding up solid-state battery development. *Nat. Energy* **2023**, *8*, 230–240.

(2) Betz, J.; Bieker, G.; Meister, P.; Placke, T.; Winter, M.; Schmuch, R. Theoretical versus practical energy: a plea for more transparency in the energy calculation of different rechargeable battery systems. *Adv. Energy Mater.* **2019**, *9*, 1803170.

(3) Zhu, L.; Wang, Y.; Chen, J.; Li, W.; Wang, T.; Wu, J.; Han, S.; Xia, Y.; Wu, Y.; Wu, M., et al. Enhancing ionic conductivity in solid electrolyte by relocating diffusion ions to under-coordination sites. *Sci. Adv.* **2022**, *8*, eabj7698.

(4) Ohno, S.; Banik, A.; Dewald, G. F.; Kraft, M. A.; Krauskopf, T.; Minafra, N.; Till, P.; Weiss, M.; Zeier, W. G. Materials design of ionic conductors for solid state batteries. *Prog. Energy.* **2020**, *2*, 022001.

(5) Liu, Y.; Wang, C.; Yoon, S. G.; Han, S. Y.; Lewis, J. A.; Prakash, D.; Klein, E. J.; Chen, T.; Kang, D. H.; Majumdar, D., et al. Aluminum foil negative electrodes with multiphase microstructure for all-solid-state Li-ion batteries. *Nat. Commun.* **2023**, *14*, 3975.

(6) Aspinall, J.; Sada, K.; Guo, H.; Kotakadi, S.; Narayanan, S.; Chart, Y.; Jagger, B.; Milan, E.; Brassart, L.; Armstrong, D., et al. The impact of magnesium content on lithium-magnesium alloy electrode performance with argyrodite solid electrolyte. *Nat. Commun.* **2024**, *15*, 4511.

(7) Wang, Z.-X.; Lu, Y.; Zhao, C.-Z.; Huang, W.-Z.; Huang, X.-Y.; Kong, W.-J.; Li, L.-X.; Wang, Z.-Y.; Yuan, H.; Huang, J.-Q., et al. Suppressing Li voids in all-solid-state lithium metal batteries through Li diffusion regulation. *Joule* **2024**, *8*, 2794–2810.

(8) Kim, J.-S.; Yoon, G.; Kim, S.; Sugata, S.; Yashiro, N.; Suzuki, S.; Lee, M.-J.; Kim, R.; Badding, M.; Song, Z., et al. Surface engineering of inorganic solid-state electrolytes via interlayers strategy for developing long-cycling quasi-all-solid-state lithium batteries. *Nat. Commun.* **2023**, *14*, 782.

(9) Sandoval, S. E.; Lewis, J. A.; Vishnugopi, B. S.; Nelson, D. L.; Schneider, M. M.; Cortes, F. J. Q.; Matthews, C. M.; Watt, J.; Tian, M.; Shevchenko, P., et al. Structural and electrochemical evolution of alloy interfacial layers in anode-free solid-state batteries. *Joule* **2023**, *7*, 2054–2073.

(10) Haslam, C. G.; Fuchs, T.; Liao, D. W.; Becker, J.; Dasgupta, N. P.; Janek, J.; Sakamoto, J. The Effect of Alloying Interlayers on Lithium Anode Morphology and Microstructure in "Anode-Free" Solid-State Batteries. *ACS Energy Lett.* **2025**, *10*, 2285–2291.

(11) Thorpe, M. A.; Zhang, M.; Liao, D. W.; Sandoval, S. E.; Kim, Y.; McDowell, M. T.; Thouless, M.; Dasgupta, N. P. Controlling stack pressure inhomogeneity in anode-free solid-state batteries using elastomeric interlayers. *Matter* **2025**, 101955.

(12) Yang, C.; Zhang, L.; Liu, B.; Xu, S.; Hamann, T.; McOwen, D.; Dai, J.; Luo, W.; Gong, Y.; Wachsman, E. D., et al. Continuous plating/stripping behavior of solid-state lithium metal anode in a 3D ion-conductive framework. *Proc. Natl. Acad. Sci. U. S. A.* **2018**, *115*, 3770–3775.

(13) Shen, H.; Yi, E.; Heywood, S.; Parkinson, D. Y.; Chen, G.; Tamura, N.; Sofie, S.; Chen, K.; Doeff, M. M. Scalable freeze-tape-casting fabrication and pore structure analysis of 3D LLZO solid-state electrolytes. *ACS Appl. Mater. Interfaces* **2019**, *12*, 3494–3501.

(14) Zhang, H.; Okur, F.; Pant, B.; Klimpel, M.; Butenko, S.; Karabay, D. T.; Parrilli, A.; Neels, A.; Cao, Y.; Kravchyk, K. V., et al. Garnet-based solid-state Li batteries with high-surface-area porous LLZO membranes. *ACS Appl. Mater. Interfaces* **2024**, *16*, 12353–12362.

(15) Alsaç, E. P.; Nelson, D. L.; Yoon, S. G.; Cavallaro, K. A.; Wang, C.; Sandoval, S. E.; Eze, U. D.; Jeong, W. J.; McDowell, M. T. Characterizing Electrode Materials and Interfaces in Solid-State Batteries. *Chem. Rev.* **2025**, *125*, 4, 2009.

(16) Koshikawa, H.; Matsuda, S.; Kamiya, K.; Miyayama, M.; Kubo, Y.; Uosaki, K.; Hashimoto, K.; Nakanishi, S. Dynamic changes in charge-transfer resistance at Li metal/$Li_7La_3Zr_2O_{12}$ interfaces during electrochemical Li dissolution/deposition cycles. *J. Power Sources* **2018**, *376*, 147–151.

(17) Krauskopf, T.; Hartmann, H.; Zeier, W. G.; Janek, J. Toward a fundamental understanding of the lithium metal anode in solid-state batteries—an electrochemo-mechanical study on the garnet-type solid electrolyte $Li_{6.25}Al_{0.25}La_3Zr_2O_{12}$. *ACS Appl. Mater. Interfaces* **2019**, *11*, 14463–14477.

(18) Shishvan, S.; Fleck, N.; McMeeking, R.; Deshpande, V. Failure mechanisms at the Li anode/solid electrolyte interface during Li stripping. *Mech. Mater.* **2024**, *193*, 104990.

(19) Roach, A. M.; Zhu, W.; Vema, S.; McMeeking, R. M.; Grey, C. P.; Deshpande, V. S.; Fleck, N. A. Void growth in the lithium anode of a solid state battery. *Eur. J. Mech. A/Solids* **2025**, 105710.

(20) Vema, S.; Gott, J.; Yin, H.; Roach, A.; West, G.; Fleck, N.; Deshpande, V.; Grey, C. Contact loss in all solid-state Li-ion batteries via deposition of impurities. *ChemRxiv* **2025**, 1.

(21) Lee, K.; Kazyak, E.; Wang, M. J.; Dasgupta, N. P.; Sakamoto, J. Analyzing void formation and rewetting of thin in situ-formed Li anodes on LLZO. *Joule* **2022**, *6*, 2547–2565.

(22) Wang, M. J.; Choudhury, R.; Sakamoto, J. Characterizing the Li-solid-electrolyte interface dynamics as a function of stack pressure and current density. *Joule* **2019**, *3*, 2165–2178.

(23) Lewis, J. A.; Cortes, F. J. Q.; Liu, Y.; Miers, J. C.; Verma, A.; Vishnugopi, B. S.; Tippens, J.; Prakash, D.; Marchese, T. S.; Han, S. Y.; Lee, C.; Shetty, P.; Lee, H.-W.; Shevchenko, P.; De Carlo, F.; Saldana, C.; Mukherjee, P.; McDowell, M. Linking void and interphase evolution to electrochemistry in solid-state batteries using operando X-ray tomography. *Nat. Mater.* **2021**, *20*, 503–510.

(24) Lu, Y.; Zhao, C.-Z.; Hu, J.-K.; Sun, S.; Yuan, H.; Fu, Z.-H.; Chen, X.; Huang, J.-Q.; Ouyang, M.; Zhang, Q. The void formation behaviors in working solid-state Li metal batteries. *Sci. Adv.* **2022**, *8*, eadd0510.

(25) Kasemchainan, J.; Zekoll, S.; Spencer Jolly, D.; Ning, Z.; Hartley, G. O.; Marrow, J.; Bruce, P. G. Critical stripping current leads to dendrite formation on plating in lithium anode solid electrolyte cells. *Nat. Mater.* **2019**, *18*, 1105–1111.

(26) Fincher, C. D.; Ojeda, D.; Zhang, Y.; Pharr, G. M.; Pharr, M. Mechanical properties of metallic lithium: from nano to bulk scales. *Acta Mater.* **2020**, *186*, 215–222.

(27) LePage, W. S.; Chen, Y.; Kazyak, E.; Chen, K.-H.; Sanchez, A. J.; Poli, A.; Arruda, E. M.; Thouless, M.; Dasgupta, N. P. Lithium mechanics: roles of strain rate and temperature and implications for lithium metal batteries. *J. Electrochem. Soc.* **2019**, *166*, A89–A97.
(28) Schmalzried, H.; Janek, J. Chemical kinetics of phase boundaries in solids. *Ber. Bunsenges. Phys. Chem.* **1998**, *102*, 127–143.
(29) Dixit, M. B.; Verma, A.; Zaman, W.; Zhong, X.; Kenesei, P.; Park, J. S.; Almer, J.; Mukherjee, P. P.; Hatzell, K. B. Synchrotron imaging of pore formation in Li metal solid-state batteries aided by machine learning. *ACS Appl. Energy Mater.* **2020**, *3*, 9534–9542.
(30) Gao, H.; Lin, C.; Liu, Y.; Shi, J.; Zhang, B.; Sun, Z.; Li, Z.; Wang, Y.; Yang, M.; Cheng, Y., et al. Galvanostatic cycling of a micron-sized solid-state battery: Visually linking void evolution to electrochemistry. *Sci. Adv.* **2025**, *11*, eadt4666.
(31) Schall, T. A.; Fuchs, T.; Eckhardt, J. K.; Klunz, T.; Mogwitz, B.; Sann, J.; Peppler, K.; Janek, J. Evolution of Pore Volume During Stripping of Lithium Metal in Solid-State Batteries Observed with Operando Dilatometry. *Small* **2025**, 2505053.
(32) Agier, J.; Shishvan, S.; Fleck, N.; Deshpande, V. Void growth within Li electrodes in solid electrolyte cells. *Acta Mater.* **2022**, *240*, 118303.
(33) Owen, R. E.; Du, W.; Millichamp, J.; Shearing, P. R.; Brett, D. J.; Robinson, J. B. Visualising the Effect of Areal Current Density on the Performance and Degradation of Lithium Sulfur Batteries Using Operando Optical Microscopy. *J. Electrochem. Soc.* **2024**, *171*, 120523.
(34) Wang, C.; Lin, R.; He, Y.; Zou, P.; Kisslinger, K.; He, Q.; Li, J.; Xin, H. L. Tension-induced cavitation in Li-metal stripping. *Adv. Mater.* **2023**, *35*, 2209091.
(35) Putra, R. P.; Matsushita, K.; Ohnishi, T.; Masuda, T. Operando nanomechanical mapping of amorphous silicon thin film electrodes in all-solid-state Lithium-ion battery configuration during electrochemical lithiation and delithiation. *J. Phys. Chem. Lett.* **2024**, *15*, 490–498.
(36) Eckhardt, J. K.; Klar, P. J.; Janek, J.; Heiliger, C. Interplay of dynamic constriction and interface morphology between reversible metal anode and solid electrolyte in solid state batteries. *ACS Appl. Mater. Interfaces.* **2022**, *14*, 35545–35554.
(37) Avadanii, D.; Ganschow, S.; Stypa, M.; Müller, S.; Lang, S.; Kramer, D.; Kirchlechner, C.; Mönig, R. Disconnected Lithium Metal Damages Solid-State Electrolytes. *ACS Energy Lett.* **2025**, *10*, 2061–2067.
(38) Reisecker, V.; Flatscher, F.; Porz, L.; Fincher, C.; Todt, J.; Hanghofer, I.; Hennige, V.; Linares-Moreau, M.; Falcaro, P.; Ganschow, S., et al. Effect of pulse-current-based protocols on the lithium dendrite formation and evolution in all-solid-state batteries. *Nat. Commun.* **2023**, *14*, 2432.
(39) Porz, L.; Swamy, T.; Sheldon, B. W.; Rettenwander, D.; Frömling, T.; Thaman, H. L.; Berendts, S.; Uecker, R.; Carter, W. C.; Chiang, Y.-M. Mechanism of lithium metal penetration through inorganic solid electrolytes. *Adv. Energy Mater.* **2017**, *7*, 1701003.
(40) Puls, S.; Nazmutdinova, E.; Kalyk, F.; Woolley, H. M.; Thomsen, J. F.; Cheng, Z.; Fauchier-Magnan, A.; Gautam, A.; Gockeln, M.; Ham, S.-Y., et al. Benchmarking the reproducibility of all-solid-state battery cell performance. *Nat. Energy* **2024**, *9*, 1310–1320.
(41) Lang, S.; Hennerici, L.; Kramer, D.; Avadanii, D.; Mück, S.; Linz, M.; Kita, J.; Moos, R.; Mönig, R. Formation, Growth, and Shrinkage of Voids in Lithium Metal in Contact With an LLZO Electrolyte. *ACS Appl. Mater. Interfaces* **2025**, *17*, 41, 56980.
(42) Swamy, T.; Park, R.; Sheldon, B. W.; Rettenwander, D.; Porz, L.; Berendts, S.; Uecker, R.; Carter, W. C.; Chiang, Y.-M. Lithium metal penetration induced by electrodeposition through solid electrolytes: example in single-crystal Li6La3ZrTaO12 garnet. *J. Electrochem. Soc.* **2018**, *165*, A3648–A3655.
(43) Porz, L.; Knez, D.; Scherer, M.; Ganschow, S.; Kothleitner, G.; Rettenwander, D. Dislocations in ceramic electrolytes for solid-state Li batteries. *Sci. Reps* **2021**, *11*, 8949.
(44) Flatscher, F.; Todt, J.; Burghammer, M.; Søreide, H.-S.; Porz, L.; Li, Y.; Wenner, S.; Bobal, V.; Ganschow, S.; Sartory, B., et al. Deflecting dendrites by introducing compressive stress in $Li_7La_3Zr_2O_{12}$ using ion implantation. *Small* **2024**, *20*, 2307515.
(45) Yildirim, C.; Flatscher, F.; Ganschow, S.; Lassnig, A.; Gammer, C.; Todt, J.; Keckes, J.; Rettenwander, D. Understanding the origin of lithium dendrite branching in Li6.5La3Zr1.5Ta0.5O12 solid-state electrolyte via microscopy measurements. *Nat. Commun.* **2024**, *15*, 8207.
(46) Smetaczek, S.; Pycha, E.; Ring, J.; Siebenhofer, M.; Ganschow, S.; Berendts, S.; Nenning, A.; Kubicek, M.; Rettenwander, D.; Limbeck, A., et al. Investigating the electrochemical stability of Li7La3Zr2O12 solid electrolytes using field stress experiments. *J. Mater. Chem. A.* **2021**, *9*, 15226–15237.
(47) Singh, D. K.; Fuchs, T.; Krempaszky, C.; Schweitzer, P.; Lerch, C.; Richter, F. H.; Janek, J. Origin of the lithium metal anode instability in solid-state batteries during discharge. *Matter* **2023**, *6*, 1463–1483.
(48) Kazyak, E.; Garcia-Mendez, R.; LePage, W. S.; Sharafi, A.; Davis, A. L.; Sanchez, A. J.; Chen, K.-H.; Haslam, C.; Sakamoto, J.; Dasgupta, N. P. Li penetration in ceramic solid electrolytes: operando microscopy analysis of morphology, propagation, and reversibility. *Matter* **2020**, *2*, 1025–1048.
(49) Zhang, H.; Ulusel, M.; Shi, F. Nucleation of Pitting and Evolution of Stripping on Lithium-Metal Anodes. *ACS Appl. Mater. Interfaces.* **2024**, *16*, 66971–66980.
(50) Barai, P.; Fuchs, T.; Trevisanello, E.; Richter, F. H.; Janek, J.; Srinivasan, V. Study of void formation at the lithium— solid electrolyte interface. *Chem. Mater.* **2024**, *36*, 2245–2258.
(51) Zhu, Y.; He, X.; Mo, Y. Origin of outstanding stability in the lithium solid electrolyte materials: insights from thermodynamic analyses based on first-principles calculations. *ACS Appl. Mater. Interfaces* **2015**, *7*, 23685–23693.
(52) Siniscalchi, M.; Gibson, J. S.; Tufnail, J.; Swallow, J. E.; Lewis, J.; Matthews, G.; Karagoz, B.; van Spronsen, M. A.; Held, G.; Weatherup, R. S., et al. Removal and Reoccurrence of LLZTO Surface Contaminants under Glovebox Conditions. *ACS Appl. Mater. Interfaces* **2024**, *16*, 27230–27241.
(53) Otto, S.-K.; Riegger, L. M.; Fuchs, T.; Kayser, S.; Schweitzer, P.; Burkhardt, S.; Henss, A.; Janek, J. In situ investigation of lithium metal–solid electrolyte anode interfaces with ToF-SIMS. *Adv. Mater. Interfaces* **2022**, *9*, 2102387.
(54) Vema, S.; Sayed, F. N.; Nagendran, S.; Karagoz, B.; Sternemann, C.; Paulus, M.; Held, G.; Grey, C. P. Understanding the surface regeneration and reactivity of garnet solid-state electrolytes. *ACS Energy Lett.* **2023**, *8*, 3476–3484.
(55) Sharafi, A.; Kazyak, E.; Davis, A. L.; Yu, S.; Thompson, T.; Siegel, D. J.; Dasgupta, N. P.; Sakamoto, J. Surface chemistry mechanism of ultra-low interfacial resistance in the solid-state electrolyte $Li_7La_3Zr_2O_{12}$. *Chem. Mater.* **2017**, *29*, 7961–7968.
(56) Otto, S.-K.; Fuchs, T.; Moryson, Y.; Lerch, C.; Mogwitz, B.; Sann, J.; Janek, J.; Henss, A. Storage of lithium metal: the role of the native passivation layer for the anode interface resistance in solid state batteries. *ACS Appl. Energy Mater.* **2021**, *4*, 12798–12807.
(57) Wang, J.; Wang, H.; Xie, J.; Yang, A.; Pei, A.; Wu, C.-L.; Shi, F.; Liu, Y.; Lin, D.; Gong, Y., et al. Fundamental study on the wetting property of liquid lithium. *Energy Storage Mater.* **2018**, *14*, 345–350.
(58) Becker, J.; Weintraut, T.; Benz, S. L.; Fuchs, T.; Lerch, C.; Becker, P.; Eckhardt, J. K.; Henß, A.; Richter, F. H.; Janek, J. Purity of lithium metal electrode and its impact on lithium stripping in solid-state batteries. *Nat. Commun.* **2025**, *16*, 5395.
(59) Zaman, W.; Zhao, L.; Martin, T.; Zhang, X.; Wang, Z.; Wang, Q. J.; Harris, S.; Hatzell, K. B. Temperature and pressure effects on unrecoverable voids in Li metal solid-state batteries. *ACS Appl. Mater. Interfaces* **2023**, *15*, 37401–37409.
(60) Park, J.; Xie, S. R.; Wu, Z.; Lawson, J. W. Electrochemical Stability and Reduction Mechanism of LLZO Interfaces in Li Batteries from First Principles. *J. Am. Chem. Soc.* **2025**, *147*, 39080–39092.
(61) Samson, A. J.; Hofstetter, K.; Bag, S.; Thangadurai, V. A bird's-eye view of Li-stuffed garnet-type $Li_7La_3Zr_2O_{12}$ ceramic electrolytes for advanced all-solid-state Li batteries. *Energy Environ. Sci.* **2019**, *12*, 2957–2975.

(62) Arzt, E.; Ashby, M. F.; Verrall, R. Interface controlled diffusional creep. *Acta Metall.* **1983**, *31*, 1977–1989.
(63) Schroeder, M.; Wolf, D. Diffusion on strained surfaces. *Surf. Sci.* **1997**, *375*, 129–140.
(64) Aspinall, J.; Armstrong, D. E.; Pasta, M. EBSD-coupled indentation: nanoscale mechanics of lithium metal. *Mater. Today Energy* **2022**, *30*, 101183.
(65) Lee, K.; Sakamoto, J. Li Stripping Behavior of Anode-Free Solid-State Batteries Under Intermittent-Current Discharge Conditions. *Adv. Energy Mater.* **2024**, *14*, 2303571.
(66) Jäckle, M.; Helmbrecht, K.; Smits, M.; Stottmeister, D.; Groß, A. Self-diffusion barriers: possible descriptors for dendrite growth in batteries? *Energy Environ. Sci.* **2018**, *11*, 3400–3407.
(67) Yoon, J. S.; Sulaimon, H.; Siegel, D. J. Exploiting grain boundary diffusion to minimize dendrite formation in lithium metal-solid state batteries. *J. Mater. Chem. A.* **2023**, *11*, 23288–23299.
(68) Haslam, C. G.; Wolfenstine, J. B.; Sakamoto, J. The effect of aspect ratio on the mechanical behavior of Li metal in solid-state cells. *J. Power Sources* **2022**, *520*, 230831.
(69) Masias, A.; Felten, N.; Garcia-Mendez, R.; Wolfenstine, J.; Sakamoto, J. Elastic, plastic, and creep mechanical properties of lithium metal. *J. Mater. Sci.* **2019**, *54*, 2585–2600.
(70) Banerjee, S.; Vishnugopi, B. S.; Mukherjee, P. P. Probing the Impact of Vacancy Diffusion on Void Dynamics at the Lithium Metal–Solid Electrolyte Interface. *Adv. Sci.* **2025**, e15827.

https://doi.org/10.1021/acsaem.6c00908
ACS Appl. Energy Mater. XXXX, XXX, XXX–XXX